Bioresource Technology 409 (2024) 131251

Contents lists available at ScienceDirect

Bioresource Technology

journal homepage: www.elsevier.com/locate/biortech

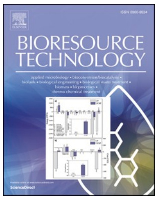

Conversion of high moisture biomass to hierarchical porous carbon via molten base carbonisation and activation for electrochemical double layer capacitor

Ishioma Laurene Egun [b,c,d], Bamidele Akinwolemiwa [b], Bo Yin [c], Hai Tian [c], Haiyong He [a,c,*], Kam Loon Fow [b], Honglei Zhang [b], George Z. Chen [e], Di Hu [b,*]

[a] *Chemistry and Chemical Engineering College, Gannan Normal University, Ganzhou, 341000, PR China*
[b] *Department of Chemical and Environmental Engineering, Faculty of Science and Engineering University of Nottingham Ningbo China, Ningbo 315100, PR China*
[c] *Ningbo Institute of Materials Technology and Engineering, Chinese Academy of Sciences, Ningbo 315201, PR China*
[d] *School of Biological and Chemical Engineering, Ningbo Tech University, Ningbo 315100, PR China*
[e] *Department of Chemical and Environmental Engineering, Faculty of Engineering, University of Nottingham, Nottingham NG7 2RD, UK*

HIGHLIGHTS

- Intercalating K^+ into biomass components and structure before drying.
- Low consumption of KOH, single-stage carbonisation and in-situ activation.
- Ultra micropores (<0.7 nm) and super micropores (0.7–2 nm) in carbon.
- Large specific surface area (1367–1948 m^2/g) without further treatment.
- Excellent electrochemical performance of 327F g^{-1} with over 10,000 cycles.
- Environmentally friendly route for conversion of high moisture biomass sources.

GRAPHICAL ABSTRACT

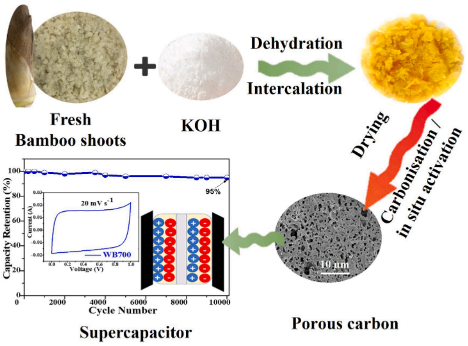

ARTICLE INFO

Keywords:
Bamboo shoots
Potassium ion
Graphitic
Ultra micropores
Heteroatoms
Specific surface area
Capacitance

ABSTRACT

Biomass-derived carbon for supercapacitors faces the challenge of achieving hierarchical porous carbon with graphitic structure and specific heteroatoms through a single-stage thermal process that minimises resource input. Herein, molten base carbonisation and activation is proposed. The process utilises the inherent moisture of Moso bamboo shoots, coupled with a low amount of KOH, to form potassium organic salts before drying. The resultant potassium salts promote in-situ activation during single-stage heating process, yielding hierarchical porous, large specific surface area, and partially graphitised carbon with heteroatoms (N, O). As an electrode material, this carbon exhibits a specific capacitance of 327F g^{-1} in 6 M KOH and 182F g^{-1} in 1 M $TEABF_4$/AN, demonstrating excellent cycling stability over 10,000 cycles at 2 A/g. Overall, this study presents a

---

* Corresponding authors.
E-mail addresses: isiegun@yahoo.com (I.L. Egun), bamidele.akinwolemiwa2@nottingham.edu.cn (B. Akinwolemiwa), Yinbo@nimte.ac.cn (B. Yin), 1225514731@qq.com (H. Tian), hehaiyong@gnnu.edu.cn (H. He), kam-loon.fow@nottingham.edu.cn (K.L. Fow), honglei-zhang@nottingham.edu.cn (H. Zhang), george.chen@nottingham.ac.uk (G.Z. Chen), di.hu@nottingham.edu.cn (D. Hu).

https://doi.org/10.1016/j.biortech.2024.131251
Received 17 May 2024; Received in revised form 5 August 2024; Accepted 7 August 2024

straightforward process that avoids pre-drying of biomass, minimises base consumption, and employs single-stage heating to fabricate electrode carbon suitable for supercapacitors.

1. Introduction

The growing demand for renewable energy is propelling advancements in energy storage technologies, particularly rechargeable batteries and electrochemical double layer (EDL) capacitors (Chung et al., 2020; Senthil et al., 2022). These devices require carbon materials with high specific surface area (SSA), optimal hierarchical porous structures, electrical conductivity, and favorable surface properties as electrode active material for superior electrochemical performance (Lyu et al., 2019; Pang et al., 2021). However, traditional carbon materials are derived from non-renewable and expensive sources, involve complex and multi-stage thermal processes that are environmentally burdensome (Sun et al., 2023). Thus, the focus is on renewable, sustainable carbon sources and their process routes.

Biomass is recognized as a sustainable carbon precursor, characterized by its high carbon content, ubiquity, economic viability, and rapid regeneration cycle (Gu et al., 2019; Lyu et al., 2019). It has been converted to various carbon materials for use as active electrode materials in lithium-ion and sodium-ion batteries (Senthil et al., 2022), electrochemical double layer capacitors (Sangtong et al., 2021), and bioelectrochemical systems (Li et al., 2020). These applications are attributed to their unique structure, naturally occurring heteroatoms, high SSA, and tuneable pore structure (Yang et al., 2019a; Huang et al., 2019).

Converting biomass into hierarchical porous carbon for electrode applications commonly involves pyrolysis, carbonisation, and hydrothermal processes (Krylova & Zaitchenko, 2018; Yang et al., 2019b), followed by activation with agents like H_3PO_4, KOH (Choudhury et al., 2022), Na_2CO_3, $ZnCl_2$ (Celiktas & Alptekin, 2019), NaOH, or LiOH (Sangtong et al., 2021), as well as molten salt carbonisation and activation (Egun et al., 2022). Currently, challenges of these process routes include drying high moisture biomass, multi-stage thermal treatments from carbonisation to activation (Sun et al., 2023), substantial reagent use during activation, e.g., typically a minimum 4:1 reagent-to-biomass char ratio (Zou et al., 2019), and the deficiency in certain properties of the derived carbon for its use in electrode applications. Therefore, developing a process that mitigates these challenges is a pivotal research focus for advancing electrochemical energy storage materials.

In this study, molten base carbonisation and activation (MBCA) is proposed as an innovative approach to address the aforementioned challenges, utilising Moso bamboo shoots (Phyllostachys edulis). This biomass is a rich carbon source, composed of lignin, hemicellulose, and cellulose, and is renowned for its rapid growth rate (Wang et al., 2022). However, its high moisture content (85 % wt.) (Poonam et al., 2018) accelerates deterioration, resulting in economic losses and environmental pollution. Therefore, the MBCA process takes advantage of this inherent moisture, combining it with a low amount of KOH to engage the biomass components in reactions forming potassium compounds through dehydration, hydrolysis, and nucleophilic substitution reactions prior to drying. These compounds promote in-situ activation at elevated temperatures during carbonisation, yielding carbon with a large SSA enriched with ultra micropores and super micropore structures. The carbon obtained at 700 °C exhibited a specific capacitance of 327F g^{-1} in 6 M KOH, demonstrating exceptional cycling stability with 95 % retention of capacitance after 10,000 cycles.

Further investigation of the MBCA process, using a dried precursor and varying process temperatures, revealed that the moisture content of the precursor and the carbonisation temperature are crucial for achieving carbon properties beneficial to enhance capacitive performance. This study underscores that effective intercalation of pore-forming ions within the wet biomass structure before drying and the selection of carbonisation temperature are critical for producing ultra micropores and supermicropores in porous carbon through a single-stage thermal process from high moisture biomass, thereby advancing carbon material development for energy storage.

2. Experimental section

2.1. Moso bamboo carbonisation process

Moso bamboo shoots (*Phyllostachys edulis*) from Ningbo, China, were shredded into 0.5 cm strips. Then 4 g of KOH was mixed with 60 g of this wet biomass (1:15 mass ratio), creating a KOH-bamboo shoots mixture termed ‘WB’. The WB was crushed, sealed, and reacted at room temperature for 48 h. Post-reaction, WB was dried at 60 °C for 24 h and ground into a fine powder using an IKA-A11BS25 mill. The powder was carbonised in a HF-Kejing OTF −1200X furnace at 700 °C for 3 h with a 5 °C min^{-1} ramp under a 150mL min^{-1} argon flow. Post-carbonisation, the sample cooled under argon, washed to pH 7, and dried at 60 °C for 12 h to yield WB700. This process was repeated at 800 °C and 900 °C, yielding WB800 and WB900, respectively. The carbon yield was calculated using equation (1), based on the dried feedstock mass post-KOH mixing.

$$Carbonyield(\%) = \frac{Mass\ of\ carbon\ recovered}{Mass\ of\ Dried\ feedstock\ fed\ to\ reactor} X100\% \qquad (1)$$

To investigate the role of moisture in the process, shredded shoot strips were dried at 60 °C for 24 h before crushing into a fine powder. KOH was then mixed with this dried powder at a KOH-to-biomass mass ratio of 1:15 and carbonised under the same conditions as WB. The carbonised sample was cooled under argon, washed to pH of 7, and dried to obtain DB700. Pristine dried shoot powder was carbonised under identical conditions without KOH, resulting in PB700.

2.2. Materials characterisation

Thermogravimetric (TGA) and differential scanning calorimetry (DSC) were conducted on precursors and derived carbon using a NETZSCH STA 449 F3 from 50 to 900 °C at 10 °C min^{-1} under argon. Elemental composition (C, H, N, and O) was assessed using an elemental analyser (Unicube, Elementar, Germany). Fourier transform infrared spectroscopy (FT-IR, Thermo Scientific Nicolet 6700) examined functional group changes from 4000 to 400 cm^{-1}. Crystallinity was evaluated using X-ray diffraction (XRD, Bruker D8 Focus) in the 5° to 80 ° 2θ range. Raman spectroscopy (Renishaw inVia, Renishaw) investigated the graphitic structure, calculating the I_D/I_G ratio from D and G peak intensities. Morphology was studied using a field emission scanning electron microscope (FE-SEM) equipped with an energy-dispersive spectrometer (EDS) (Quanta FEG 250). SSA and pore structure were analysed using a Micromeritics ASAP 2020 HD 88. Chemical composition was determined by X-ray photoelectron spectroscopy (XPS, Kratos AXIS Ultra TF20, Al Kα source).

2.3. Electrode preparation and electrochemical measurements

The carbon materials were fabricated into electrodes by blending with carbon black and polyvinylidene fluoride (PVDF), both from Aladdin Biochemical Technology Co., Ltd., in an 8:1:1 ratio. N-methyl-2-pyrrolidone (NMP) from the same supplier served as a dispersant. The slurry was coated onto 16 mm nickel foam discs, dried at 80 °C for 12 h under vacuum, and pressed at 10 MPa to achieve a 7 mg active material load. Two-electrode CR2032 coin cells were assembled using Whatman

GF/D filter paper and 6 M KOH or 1 M $TEABF_4$/AN electrolyte. The optimised carbon sample underwent three-electrode testing with a nickel foam electrode (1 cm x 1 cm, 7 mg active material loading), platinum counter electrode, and Hg/HgO reference, using a Solartron 4070E for cyclic voltammetry (CV) (5 to 200 mV/s), electrochemical impedance spectroscopy (EIS) (10 mV, 0.1 to 100 kHz), and Galvanostatic Charge/Discharge (GCD) (0.1 to 2 A/g) on a LandCT2001 device. Specific capacitance of the derived carbon in a two-electrode configuration was determined from CV and GCD profile using equations (2) and (3). The specific energy and power for devices were calculated using equations (4) and (5) (You et al., 2018; Sangtong et al., 2021).

$$C(Fg^{-1}) = 4\frac{\int Idv}{m\Delta V} \tag{2}$$

where, m (g) is the mass of active material on both electrodes, I (A) the current response, v is the scan rate (mVs^{-1}), and ΔV(V) the voltage window.

$$C(Fg^{-1}) = 4\frac{\mathrm{I}\,\Delta \mathrm{t}}{\mathrm{m}\,\Delta \mathrm{V}} \tag{3}$$

where, I (A) is the current of the cell, m (g) the mass of active material in both electrodes, ΔV(V) the voltage window, and Δt (s) the discharge time.

$$E\left(Whkg^{-1}\right) = \frac{C\Delta V^2}{2 \times 3.6} \tag{4}$$

where, C (F g^{-1}) is the specific capacitance from GCD profile, ΔV(V) the voltage window.

$$P\left(Wkg^{-1}\right) = \frac{E \times 3600}{t} \tag{5}$$

where, E (Wh kg^{-1}) is the specific energy, and t (s) the discharge time.

To investigate between capacitive and capacitive-faradaic (in this case linear pseudo-capacitance) contributions, Trasatti method was applied (Sun et al., 2023). The total capacitance is expressed in equation (6):

$$C_t = C_{EDL} + C_{pseudo} \tag{6}$$

where, C_t represents the total capacitance, which is the sum of the electrical double layer capacitance (C_{EDL}) and the pseudo-capacitance (C_{pseudo}).

The capacitance measured at a specific scan rate (C) can be expressed using the following equations (7) and (8):

$$C^{-1} = constant\ \ v^{1/2} + C_t^{-1} \tag{7}$$

In this context, C, v and C_t represent calculated capacitance, scan rate and maximum capacitance, respectively. The term "maximum capacitance (C_t)" is defined as the sum of the electrical double layer capacitance and pseudo-capacitance, as described by equation (6). This sum is determined from the reciprocal of the y-intercept of the plot of C^{-1} vs. $v^{1/2}$.

The maximum contribution for C_{EDL} can be obtained from the equation (8):

$$C = constant\ \ v^{-1/2} + C_{EDL} \tag{8}$$

where, C, v and C_{EDL} represent the calculated capacitance, scan rate, and maximum electrical double layer capacitance, respectively. The C_{EDL} is determined from the intercept of the plot of C vs. $v^{-1/2}$.

The capacitance contribution can be evaluated according to equations (9) and (10):

$$C_{EDL}\% = \frac{C_{EDL}}{C_t} \times 100\% \tag{9}$$

$$C_{pseudo}\% = \frac{C_{pseudo}}{C_t} \times 100\% \tag{10}$$

where, C_{EDL} % and C_{pseudo} % denote the respective percentages of capacitance contributed by the electrical double layer and pseudo-capacitance.

3. Results and discussion

3.1. Precursors characterisation and process investigation

The illustration of the MBCA process is shown in Fig. 1**a**. To understand the effects of inherent moisture and the interaction of KOH with components, the microstructure, crystal structure, and functional groups of PB, WB, and DB were characterised using SEM, XRD, and FT-IR. SEM micrographs (Fig. 1**b-d**) revealed structural changes in various samples with WB displaying a large distortion from inherent structure. The collapse of the vascular bundle structures in WB (Fig. 1**b)** suggests the breakdown of components, such as lignin, hemicellulose, and cellulose due to KOH and moisture interaction. This behaviour suggests that the inherent moisture facilitated the splitting of KOH into (K^+ and OH^-) that enhances faster dehydration, hydrolysis, and intercalation of K^+ ions in various components. These reactions would further expose more cellulose that may be trapped within the lignin structure, as cellulose is a rich carbon source (Ghazanfar et al., 2022). This result shows that the natural biomass recalcitrance, which poses a challenge to obtaining hierarchical porous carbon, can be reduced prior to drying. On the contrary, DB (Fig. 1**c)** showed a vascular bundle structure like PB (Fig. 1**d**), the less distortion compared to WB (Fig. 1**b**) could be ascribed to the limited reactivity of KOH with components in its dried state. These significant differences in microstructures provides new insights that inherent moisture of biomass affects its components reactivity with K^+ ions.

To confirm the extent of K^+ ion diffusion within biomass components, EDS was conducted (see supplementary material). The increased weight ratio of K^+ from 0.36 wt% in PB to 12.28 wt% in DB, and further to 42.91 wt% in WB, demonstrated that the inherent moisture promoted ion diffusion, leading to a more homogeneous distribution of K^+ within the components structure. Additionally, the colour change (Fig. 1**a**) indicates that oxidation reactions also occur at room temperature, as yellowing phenomenon in cellulose have been linked to the oxidation of carboxyl or carbonyl groups (Ahn et al., 2019).

To further confirm changes in components structure and crystallinity, XRD analysis was conducted. The XRD patterns of PB and DB (Fig. 1**e)** exhibited a broad peak at $2\theta = 21.63^\circ$, indexed to (0 0 2) plane, characteristic of amorphous cellulose (Wan, et al., 2015). The lower intensity of this peak in DB further confirms that interactions occur between KOH and dried biomass components, in agreement with SEM (Fig. 1**b)** In contrast, the absence of this peak and emergence of multiple crystalline peaks in WB, suggests the formation of new compounds linked to distortion of various O-H weak bonds in cellulose, reaction of K^+ ions with various active oxygen sites and water molecules during the alkalinisation process (Ghazanfar et al., 2022). Furthermore, intercalation of K^+ ions within the components may result to the formation of various potassium organic salts via nucleophilic reactions between KOH and C=O and COOH groups. Examples of such plausible potassium organic salts include potassium formate ($CHKO_2$), potassium hydrogen oxalate (C_2HKO_4), and potassium tartrate dihydrate ($C_4H_5O_6K_2{\cdot}2H_2O$). These are linked to oxalic acid, tartaric acid, formic acid, and other organic acids in bamboo shoots (Chen et al., 2022). It is worth noting that these potentially derived potassium salts are the building blocks of the MBCA process, as these derived potassium salts are expected to decompose and promote in-situ activation when subjected to elevated temperatures. Thus, influencing the porous structure and other properties of derived carbon.

To further investigate the influence of KOH and moisture on the

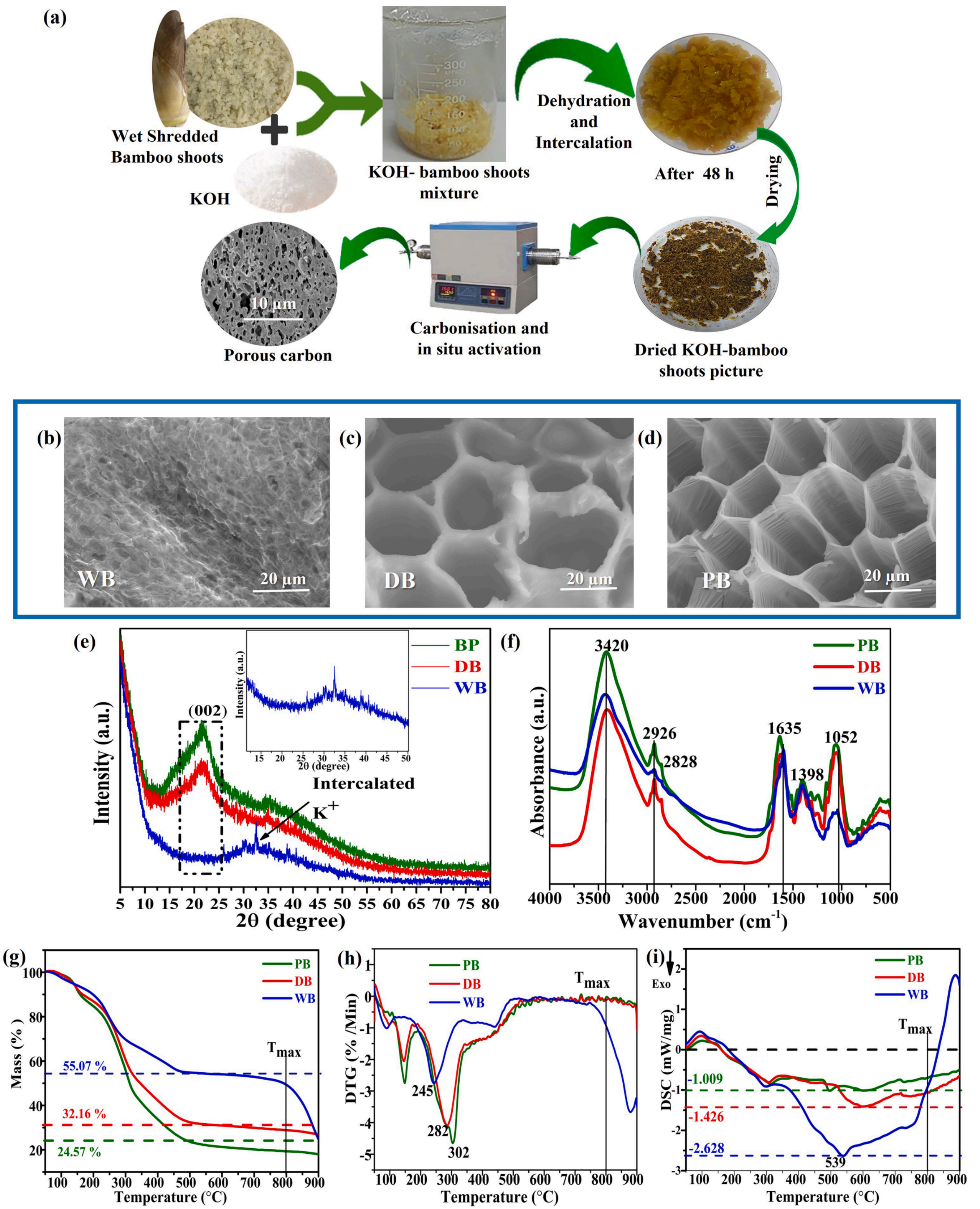

Fig. 1. (a) A detailed illustration of the novel MBCA approach for fabricating porous carbon via single-stage thermal process. FE-SEM micrographs: (b) wet bamboo shoots mixed with KOH (WB), (c) pristine dried bamboo shoots mixed with KOH (DB), and (d) pristine dried bamboo shoots (PB). (e) XRD patterns of PB, DB, and WB, with an inset of expanded view of WB pattern, (f) FTIR spectra, (g) TG curves, (h) DTG curves, and (i) DSC curves.

functional groups of PB, DB, and WB precursors, FT-IR analysis was conducted, and spectra shown in Fig. 1f. The spectra showed minimal shifts in functional group positions, indicating that functional groups are largely unaffected by KOH and moisture interactions. However, the reduced intensities in WB suggest internal compound rearrangements. Notably, WB showed decreased absorbance at 3420 cm^{-1} for hydroxyl groups (O-H), suggesting dehydration and removal of O-H groups during drying process. Also, the C-H stretch at 2900 cm^{-1} in WB exhibited a downward shift, potentially due to accelerated deacetylation and monomer decomposition influenced by KOH presence. The band shift from 1750 to 1600 cm^{-1} in WB, associated with conjugated ketones/aldehydes, suggests carboxylate reactions from interactions between KOH and active O-containing groups like C-OH and COOH (Ghazanfar et al., 2022). In addition, the lowest intensity for WB at 1052 cm^{-1} associated with C-O vibrations in cellulose alcohol, suggests reactions at weak hydrogen bonds and loss of C-O groups, which aligns with XRD findings (Fig. 1**e). These functional changes are likely to alter the degradation pattern of components when subjected to elevated temperatures and the properties of resulting carbon.

TGA analysis of PB, DB, and WB was conducted with profiles shown in Fig. 1**g-i**. Samples exhibited varying thermal responses with increasing temperature (Fig. 1**g**), which can be attributed to the structural changes in their respective compositions, earlier observed (Fig. 1**e**). The minor mass loss for all samples at 100–150 °C indicate the presence of residual moisture within the components. From 200 to 500 °C, a major mass loss was observed. This is associated with the volatilisation and decomposition of hemicellulose, cellulose, and lignin (Ghazanfar et al., 2022). However, the maximum decomposition for WB within this temperature range, suggests that K^+ intercalation in components accelerates conversion reactions. This behaviour was reflected with degradation peak at 245 °C, compared to 292 °C and 302 °C for PB and DB respectively in DTG profile (Fig. 1h). Between 300 and 500 °C, WB displayed less mass loss, suggesting potassium compounds like K_2CO_3 and K_2O may have hindered volatile release, contrasting typical biomass pyrolysis that involves gas emission within this temperature range (Liu et al., 2024). From 500 to 700 °C, all samples showed similar patterns, ascribed to common lignin reactions and carbon ring formation. Above 700 °C (**Fig. 1**g), WB exhibited substantial mass loss, particularly at 800 °C with over 20 % loss, which reflects the reactivity of K^+ with carbon at high temperature. The absence of this pattern in DB and PB, highlights the impact of K^+ intercalation and potassium-carbon component reactivity on carbon skeleton integrity. The DSC analysis (Fig. 1**i**) shows WB with the lowest heat flow (-2.628 mW mg^{-1}), compared to -1.426 mW mg^{-1} and -1.009 mW mg^{-1} for DB and PB, respectively. This reduced heat flow for WB transformation confirms that K^+ intercalation within components promotes energy conservation, which is an advantage of the MBCA process.

3.2. *Carbon characterisation*

The yield of the derived carbon calculated using equation (1) alongside their elemental composition analysis is given in Table 1. WB700 exhibited a lower carbon yield compared to DB700 and PB700, aligning with TGA (Fig. 1**g**). The results implies that pre-drying biomass reduces component reactivity during carbonisation. Also, the presence of K^+ in WB promotes the release of organic compounds at certain temperatures. As carbonisation temperature increased, carbon yield of WB800 and WB900 decreased. These findings reflect that temperature enhanced K^+ and carbon reactivity, affecting the overall carbon yield. On the contrary, the elemental carbon content increased to 76.28 % in WB800 but reduced to 75.82 % in WB900, linked to excessive reactivity of K^+ and carbon that results to carbon loss (Shen, 2018; Zhu et al., 2023). Thus, 800 °C is the ideal temperature for maximising carbon content in the MBCA process, aligning with T_{max} in the TGA profile (Fig. 1**g**). Despite the lower yield for this novel approach, the high elemental carbon content in WB700, WB800, and WB900 (Table 1) is notable compared to the 39 % inherent carbon composition in bamboo shoots (see supplementary materials). These results highlight the efficiency of the MBCA process in producing high elemental carbon material for electrode applications via a single-stage thermal process. From an environmental sustainability perspective, the targeted feedstock for this process is recognised for its rapid growth rate. Therefore, the low carbon yield is mitigated by the abundance of the feedstock, offsetting the concerns about the yield.

Further analysis of elemental composition revealed the presence of nitrogen and oxygen. WB700 had lower nitrogen and oxygen content compared to DB700 and PB700, which indicates that K^+ intercalation in the precursor facilitated deoxygenation and carboxylation reactions during carbonisation (Hu et al., 2022; Shen, 2018). This behaviour is supported by the thermal stability exhibited by WB700 with reduced mass loss in the TGA profile (see supplementary materials). In addition, the highest oxygen and nitrogen content showed by WB700 among WB800 and WB900 (Table 1**)**, shows that elevated temperatures promoted the removal of oxygen and nitrogen heteroatoms linked to carbon rearrangement. This difference in the oxygen and nitrogen content of the derived carbon is anticipated to affect its electronic properties. It is expected to improve the electro-adsorption and desorption processes through hydrogen bond interactions, which is likely to introduce a capacitive faradaic mechanism in supercapacitor applications (Li et al, 2017; Tekin & Topcu, 2024).

To investigate pore structure regulation, SEM images were collected for samples (Fig. 2). WB700 showed a hierarchical porous sheet-like structure (Fig. 2a), depicting that in-situ activation occurred, linked to the decomposition of potassium organic salts in the precursors (Fig. 1**e**) to form K^+ and CO_2, which further react to form K_2CO_3 and generate pores from in-situ activation reactions. These potassium salts have shown to be as self-activators, creating a porous structure through redox

Table 1
Carbon yield [a], elemental composition [b], specific surface area, and pore parameters [c] of various derived carbons.

Sample	Yield (%)	C	H	N	O**	S_{BET} (m^2g^{-1})	S_{BETmic} (m^2g^{-1})	$S_{BETmeso}$ (m^2/g)	V_t (cm^3g^{-1})	V_{mic} ($cm^3\ g^{-1}$)	D_A (nm)
PB700	28.00 ± 0.02	58.56 ± 0.02	1.95 ± 0.02	4.14 ± 0.02	35.35 ± 0.04	0.58 ± 0.01	0.03 ± 0.01	0.54 ± 0.01	0.00 ± 0.01	0.00 ± 0.01	6.82 ± 0.01
DB700	23.80 ± 0.02	59.23 ± 0.02	1.99 ± 0.02	3.14 ± 0.02	35.64 ± 0.04	96.49 ± 0.01	86.32 ± 0.01	10.16 ± 0.01	0.05 ± 0.01	0.04 ± 0.01	2.08 ± 0.01
WB700	8.60 ± 0.02	75.03 ± 0.02	1.71 ± 0.02	0.95 ± 0.02	22.31 ± 0.04	1367.82 ± 0.01	1137.95 ± 0.01	229.87 ± 0.01	0.66 ± 0.01	0.53 ± 0.01	1.94 ± 0.01
WB800	4.56 ± 0.02	76.28 ± 0.02	1.30 ± 0.02	0.62 ± 0.02	21.80 ± 0.04	1948.85 ± 0.01	1558.46 ± 0.01	511.27 ± 0.01	1.08 ± 0.01	0.16 ± 0.01	2.22 ± 0.01
WB900	3.73 ± 0.02	75.82 ± 0.02	1.51 ± 0.02	0.38 ± 0.02	22.03 ± 0.04	1011.11 ± 0.01	734.33 ± 0.01	199.09 ± 0.01	0.58 ± 0.01	0.15 ± 0.01	2.29 ± 0.01

[a] Results for yield, [b] ultimate analysis ** Oxygen value, calculated by difference from (100 % − C − H − N), [c] $\mathbf{S_{BET}}$ = BET Specific Surface Area, $\mathbf{S_{BETmic}}$ = Micropore Surface Area, $\mathbf{S_{BETmeso}}$ = Mesopore Surface Area, V_t = Total pore Volume, $\mathbf{V_{mic}}$ = micropore volume, and $\mathbf{D_A}$ = Average Pore size. Results are the averages and standard errors of triplicate tests [a,b]. Results are the averages and standard errors of duplicate tests [c].

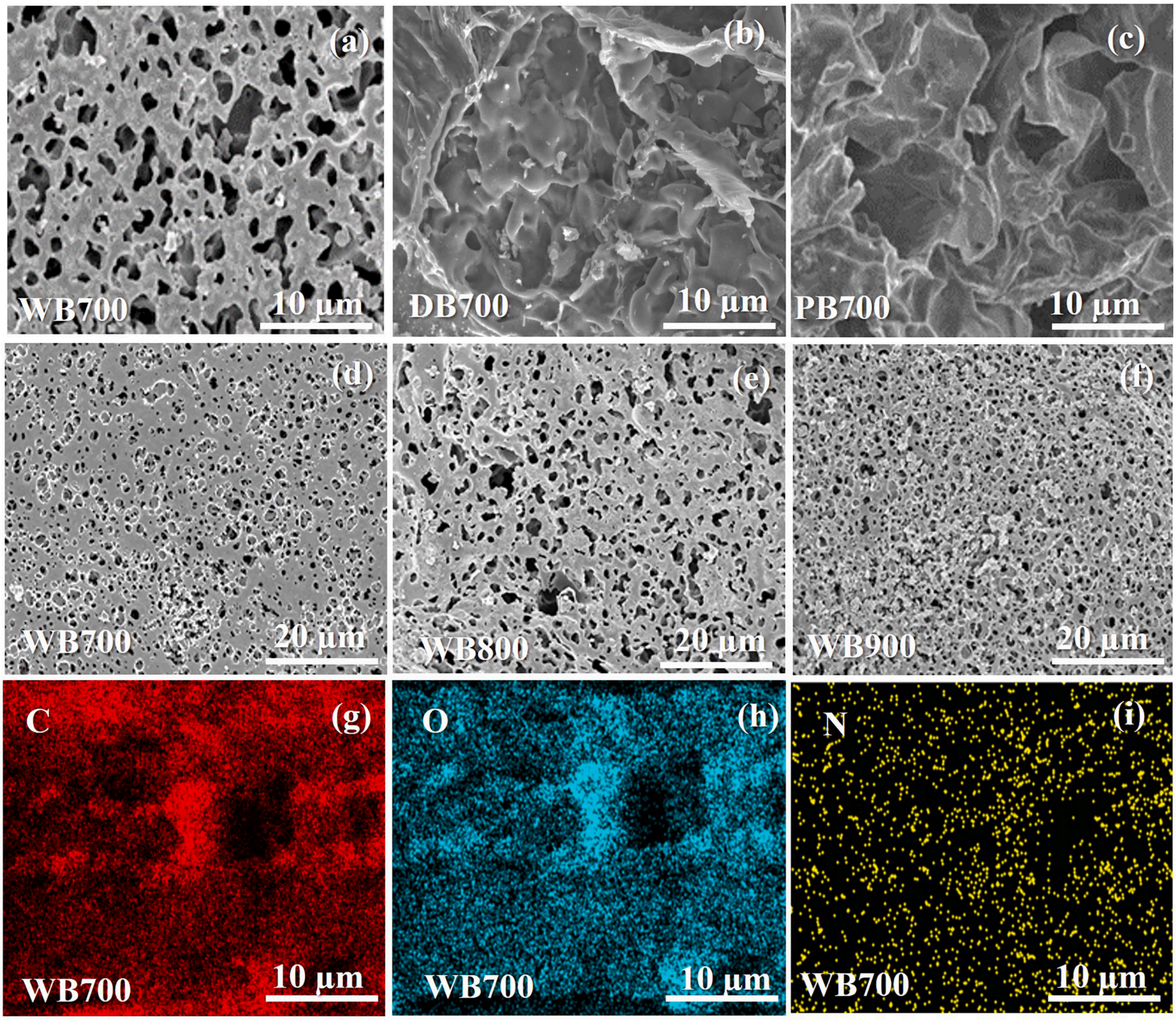

Fig. 2. FE-SEM micrographs of various derived carbon materials: (a) WB700, (b) DB700, (c) PB700, (d) WB700 (higher magnification), (e) WB800, (f) WB900, and (g-i) elemental analysis of WB700 showing C, O, and N.

reactions at elevated temperatures (Luo et al., 2015; Zhu et al., 2018). On the other hand, DB700 had a bulk-packed sheet structure with few pores (Fig. 2b), indicating that the presence of KOH in biomass during carbonisation causes formation of pores, but the complex structures might restrict the reactivity. PB700 exhibits a dense, bulky structure without visible pores (Fig. 2c), indicating that no in situ activation occurred due to lack of KOH. The results confirm that the MBCA process, using wet biomass would yield a porous carbon in a single thermal stage. SEM images of WB800 and WB900 (Fig. 2 **e-f**) were similar to that of WB700 (Fig. 2**d**) in terms of porous structure, linked to similar precursors and reactions. However, the larger pore sizes observed in WB800 and WB900 are potentially due to the reactivity of K^+ and carbon fragments at temperatures above 700 °C, which can transform micropores into mesopores (Huang et al., 2019). These findings underscore the critical role of carbonisation temperature in the development of porous structures in carbon through the MBCA process.

N_2 adsorption–desorption tests were performed to assess the porous structure of the carbon materials, with isotherms shown in Fig. 3a and porosity parameters in Table 1. From Fig. 3a, WB700 displayed a Type I isotherm with a knee bend at a relative pressure (p/p_0) below 0.2, indicating a high presence of micropores (Cao et al., 2019). DB700 exhibited low nitrogen adsorption, indicating a low presence of micropores, while PB700 showed no adsorption capacity, indicating the absence of micropores and consequently a low SSA (You et al., 2018). The lack of pores in PB700 implies that single-stage heating without a pore-forming agent results in non-porous carbon due to the presence of large molecular compounds. Furthermore, the low adsorption in DB700 suggests that dried biomass precursor would require more pore-forming reagent to overcome biomass recalcitrance. This finding aligns with the different porous structures seen in their SEM images (Fig. 2) and confirms that the dehydration, hydrolysis reactions, and intercalation of K^+ facilitated by moisture changed the rigidity of structural components, thereby promoting the formation of pores and retaining of internal voids during carbonisation. Significantly, WB800 and WB900 exhibit knee bend isotherm with relative pressure (p/p_0) up to 0.4, suggesting the presence of larger micropores and small mesopores aligning with SEM images (Fig. 2 **e-f**). However, the H1 hysteresis loop observed only in WB800 suggests the coexistence of micropores and mesopores, that resulted from micropore collapse linked to potassium reactivity with increase in temperature (Huang et al., 2019; You et al., 2018). Further SSA analysis (Table 1) reveals that WB700 has higher value of 1367.82 m^2/g compared to 96.49 m^2/g for DB700 and 0.58 m^2/g for PB700.

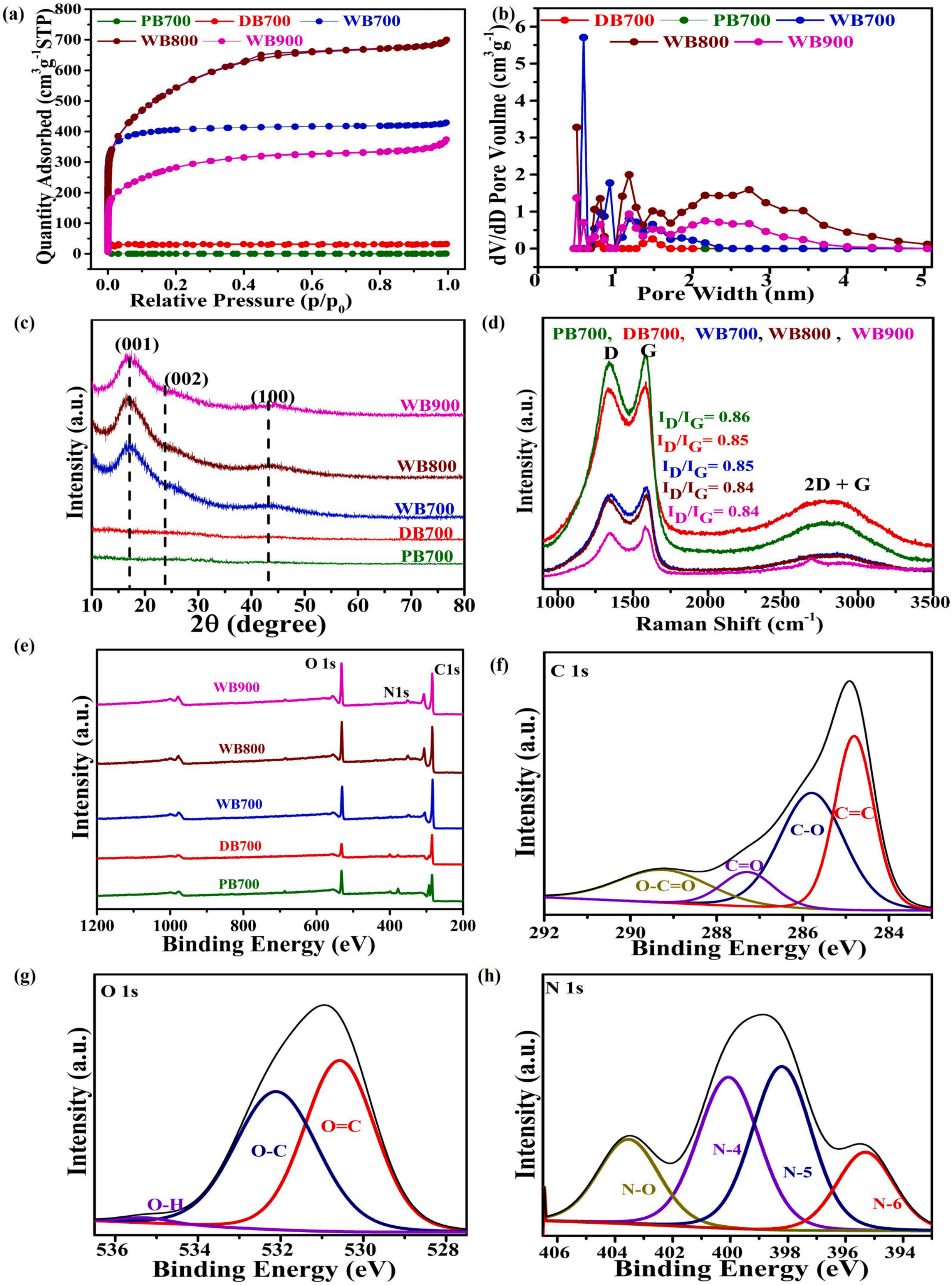

Fig. 3. (a) Nitrogen adsorption–desorption isotherms, (b) Pore size distribution, with an inset showing an expanded view, (c) XRD patterns, (d) Raman Spectra, (e) XPS survey scan spectra for PB700, DB700, WB700, WB800, and WB900, and deconvoluted spectra for WB700 of (f) C 1 s, (g) O 1 s, and (h) N 1 s.

These results highlight the role of intercalated K^+ in changing the biomass structure, which aids in the removal of rigid structures and contributes to the production of carbon with large SSA. With temperature increase, the SSA increased to 1948.85 m^2/g for WB800 but decreased to 1011.11 m^2/g for WB900. The reduced SSA of WB900 is linked to increased mesopore in carbon. Notably, the SSAs of WB700, WB800, and WB900 are critical for electrode carbon materials in EDL applications, as they are crucial for electrolyte ion adsorption, towards achieving high capacitive performance (Huang et al., 2019; Pang et al., 2021; Sun et al., 2023). However, it should be noted that beyond SSA, the pore sizes and structure will affect their charge storage capacity, thus affecting overall capacitive performance (Sangtong et al., 2021, Pang et al., 2021).

Further analysis of the pore size (Fig. 3b) revealed the presence of ultra micropores (<0.7 nm), supermicropores (0.7–2 nm), and mesopores (2–50 nm) (Zdravkov, et al., 2007). Among all the samples, WB700 displayed the highest proportion of ultra micropores (<0.7 nm) aligning with its high micropore volume (V_{mic}) of 0.53 cm^3 g^{-1} (Table 1**)**. The smaller pore size for WB700 reveals that pores in carbon are formed below 800 °C due to the formation of K_2CO_3 which promotes in-situ activation. These results imply that K^+ intercalation within components before drying helps to preserve nano pores in derived carbon. These ultra-micropores and super micropores in WB700 are expected to be helpful for adsorption and diffusion of solvated electrolyte ions. With increased temperature, the pore sizes increased (Table 1), which is ascribed to the collapse of micropores from heightened carbon and potassium reactivity. The smaller pore sizes in WB700 are anticipated to improve its capacitance in EDL application, as electrolyte-solvated ions of small sizes, such as K^+ (0.33 nm) and OH^- (0.30 nm), have shown to enhance capacitive performance with matching pore sizes (Simon & Gogotsi, 2013; Zhong et al., 2015). While mesopores in WB800 and WB900 would facilitate rapid ion transport and act as ion reservoirs (Choudhury et al., 2022; Pang et al., 2021). It should be noted that mesopores without proper internal micropore connections would limit electrochemically assessable pores for electrolyte ions, thereby reducing capacitive performance of carbon. This result further implies that 700 °C is the optimum temperature for producing ultra micropores and super micropores carbon from biomass via MBCA.

The crystallinity of carbon samples affects their hybridisation and electronic conductivity, therefore XRD was conducted, and patterns shown in Fig. 3**c.** WB700 exhibited broad peaks at 2θ degree of 17.0°, 23.9°, and 43.0°, corresponding to (0 0 1), (0 0 2) and (1 0 0) planes of graphene oxide and graphitic amorphous carbon with a turbostratic structure respectively (Bhaumik et al., 2017; Shen, 2018). However, the absence of these peaks in DB700 and PB700 indicates that K^+ intercalation in the precursor enhances the formation of graphite-like carbon layers (Cao et al., 2019). With increasing carbonisation temperature, the (0 0 1) plane shifts towards the (0 0 2) plane, indicating increased ordering of sp^2 carbon atoms and partial graphitisation, which is beneficial for enhancing electrical conductivity in carbon towards electrode applications (Sun et al., 2023). Further investigation of the graphitic structure with Raman spectroscopy shown in Fig. 3**d,** revealed peaks at 1350, 1586, and 2650 – 2925 cm^{-1}, ascribed to the D band (disordered carbon), G band (graphitic carbon), and 2D+G band (2-dimensional carbon structure), respectively (Cao et al., 2019). The I_D/I_G ratio, which shows the level of disorder and graphitic structure was calculated for samples. WB700 and DB700 revealed an I_D/I_G ratio of 0.85, compared to 0.86 for PB700, suggesting that K^+ presence during carbonisation promotes formation of graphitic crystallite (Cao et al., 2019). Upon increasing the temperature, WB900 exhibited a sharp peak around 2600 cm^{-1}, indicating an increased number of sp^2 carbon atoms and a decreased I_D/I_G ratio of 0.84. This confirms that an increase in temperature enhances the formation of graphitic structures in agreement with the XRD patterns (Fig. 3c). The enhanced graphitisation in carbon samples is expected to reduce their resistivity (see supplementary materials) and improve their electrical conductivity.

XPS was conducted to determine the chemical composition of the carbon samples, with the spectra shown in Fig. 3**e.** All samples showed different peak intensities for carbon, nitrogen, and oxygen, aligning with elemental analysis in Table 1. Deconvolution of the C 1 s peak for all samples revealed different peak positions ascribed to –C=C–, C-C-, –C=O–, O–C=O, and –C–OH (Huang et al., 2019; Ilnicka et al., 2021) as seen in Fig. 3**f** and (see supplementary). Notably, WB700 lacked the O=C=O functional group, which indicates that K^+ in the precursor promoted dehydration, deoxygenation, and decarboxylation reactions (Chen et al., 2020). This result is consistent with its lower oxygen content in elemental composition analysis **(**Table 1**)**. With increased carbonisation temperature, only WB700 exhibited the –O-C=O group, suggesting that higher temperatures further promote decarboxylation and deoxygenation, leading to carbon and oxygen loss (Chen et al., 2020). The presence of this functional group in WB700 is expected to enhance adsorption and wettability of electrolyte in electrode applications due to its partial negative charge (Tekin & Topcu, 2024; Wei & Jia, 2015). Deconvoluted oxygen peaks corresponding to O=C, O-C, O-C=O, O-C-O, and –COOH groups were observed across samples (Huang et al., 2019; Ilnicka et al., 2021; Tekin & Topcu, 2024). However, WB700 showed a reduced area for hydroxyl groups (O-H) (Fig. 3**g**) compared to DB700 and PB, correlating with its TGA profile's lower volatile content (see supplementary materials). Notably, the increased content of hydroxyl and carbonyl groups in WB700 among WB800 and WB900 is expected to give rise to linear pseudo-capacitance contribution in supercapacitor application (Li et al, 2017, Chen, 2021). This behaviour would result from electrolyte ions interactions with carbon surface groups without charge transfer thus increasing its capacitive performance (Chung et al., 2020; Ilnicka et al., 2021).

The deconvolution of the N1s peak in WB700 (Fig. 3**h**) revealed peaks corresponding to pyridinic-nitrogen (N-6), pyrrolic-nitrogen (N-5), quaternary nitrogen (N-4), and nitrogen oxide (N-O) (Huang et al., 2019; Zou et al., 2018). Specifically, N-6 and N-O at the edges of carbon structure, along with a uniform distribution of nitrogen groups, can influence its electronic properties (Pang et al., 2021; Zou et al., 2018). As carbonisation temperature increased, change in nitrogen composition was observed in WB800 and WB900 (see supplementary materials). The observed changes in nitrogen compositions for samples, are ascribed to release of volatiles and carbon rearrangement with increase in reaction temperature, aligning with elemental analysis (Table 1). These differences in nitrogen ratios for derived carbon is likely to either contribute or affect their electrochemical performance. Consequently, derived carbons from the novel MBCA process are promising materials for electrode applications in EDL capacitors. This is attributed to their large SSA, porous structure, partially graphitised structure, and the incorporation of nitrogen and oxygen heteroatoms (Huang et al., 2019; Pang et al., 2021).

3.3. Electrochemical performance

Derived porous carbons were utilised as electrode materials to fabricate symmetric supercapacitors. Using CV at a scan rate of 20 mV s^{-1} (Fig. 4**a),** WB700, WB800, and WB900 displayed a broad rectangular shape with no redox peaks, indicative of a predominantly EDL capacitive mechanism (Li et al., 2021; Tekin & Topcu, 2024). In contrast, DB700 and PB700 exhibited non-rectangular CVs with small humps, reflecting their low SSAs and increased heteroatom contents that promote faradaic reactions. The notable largest CV area for WB700 among other samples suggests its exceptional capacitive performance. The calculated specific capacitance using equation (2) at a scan rate of 20 mV/s was 79, 98, 306, 200 and 168F g^{-1} for PB700, DB700, WB700, WB800, and WB900, respectively. The high specific capacitance of WB700 is attributed to its increased electrochemically accessible surface area, which is linked to its high micropore volume (0.5267 cm^3 g^{-1}) and optimal pore size (Fig. 3**b** and Table 1). Furthermore, the presence of high ultra micropores (<0.7 nm) in WB700 is significant for effective electrolyte ion

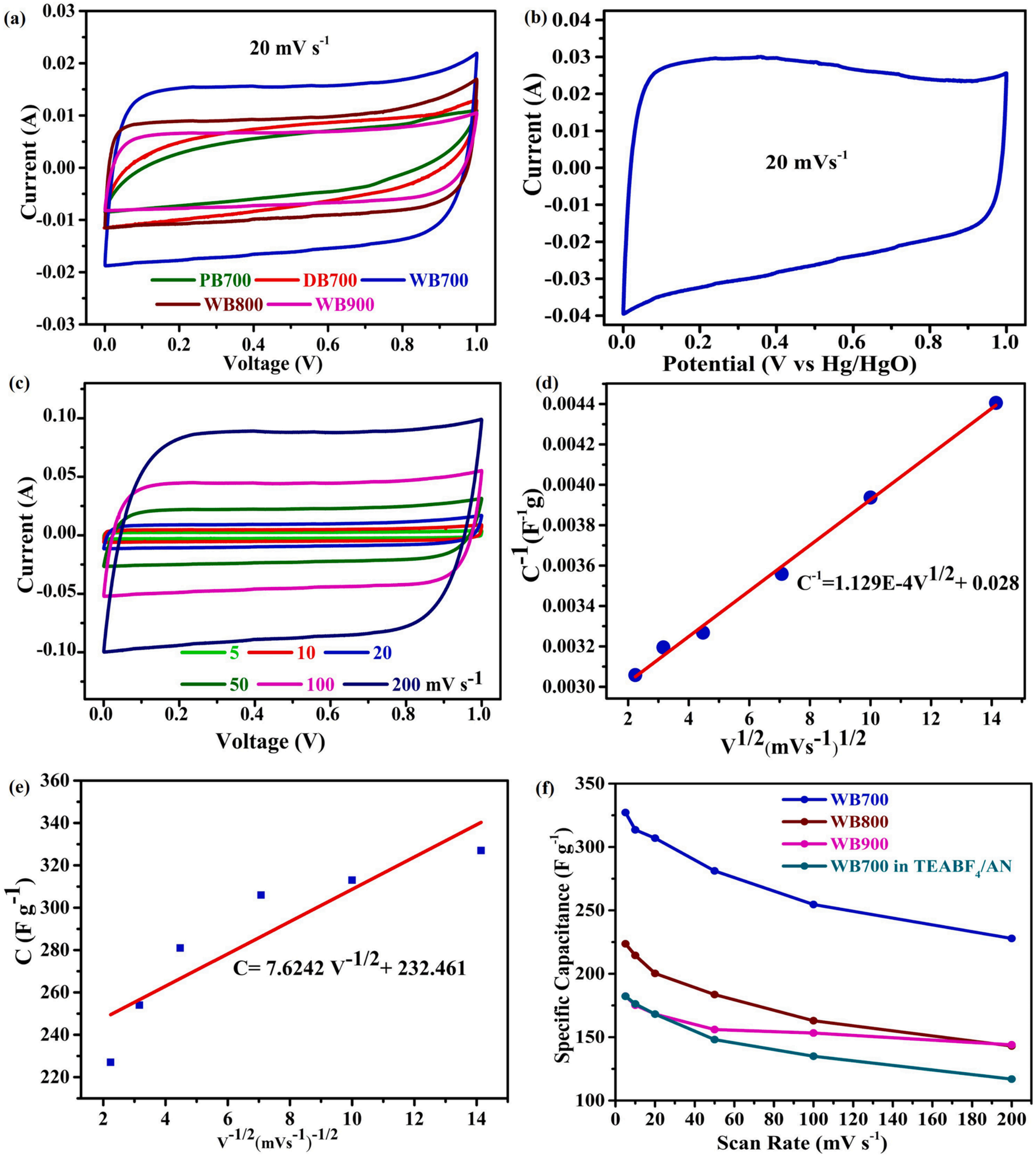

Fig. 4. (a) Comparative CVs of PB700, DB700, WB700, WB800, and WB900 at a scan rate of 20 mV/s, (b) Three-electrode CV for WB700 at 20 mV/s, (c) CVs of WB700 at various scan rates from 5 to 200 mV/s in 6 M KOH, (d) Plot of C^{-1} vs. $\nu^{1/2}$, (e) Plot of C vs. $\nu^{-1/2}$, and (f) Calculated specific capacitance from cyclic voltammetry for WB700, WB800, and WB900 at various scan rates in 6 M KOH, and for WB700 in 1 M $TEABF_4$/AN.

interaction for K^+ and OH^-, which have hydrated shell sizes of 0.33 nm and 0.30 nm, respectively (Zhong, et al., 2015), thereby promoting enhanced capacitive performance. On the contrary, the reduced capacitance of WB800 compared to that of WB700, despite its largest SSA, highlights the significance of interconnected pore structures over SSA in achieving a high electrochemically accessible area. This is essential for achieving a high capacitive performance. Similar observations regarding larger SSA and lower capacitance have been reported (Sangtong et al., 2021). Furthermore, the increased capacitive performance of WB700 could be linked to its oxygenated group in terms of the hydroxyl, carboxyl and carbonyl groups which would promote linear pseudo-capacitive mechanism in carbon to enhance its capacitive performance (Li et al, 2017, Chen, 2021). The high capacitive performance of WB700, substantiates the feasibility of deriving capacitive carbon via the MBCA process with minimal amount of KOH from wet feedstocks at lower temperature.

Based on the specific capacitance displayed by WB700, further investigation into its charge storage mechanism was conducted using a three-electrode setup with 6 M KOH. CV at 20 mVs^{-1} revealed a broad rectangular-shaped curve devoid of redox peaks (Fig. 4**b)**, affirming the dominance of the EDL capacitive mechanism. Notably, the observed increased current response between 0 and 0.4 (V vs. Hg/HgO) potential window indicates the presence of capacitive faradaic mechanism which is termed linear pseudo-capacitance. This behaviour arises from the interactions between the electrolyte and oxygen-containing functional groups on the carbon electrode surface (Li et al, 2017; Ilnicka et al., 2021). The calculated specific capacitance of 335F g^{-1} is close to 306F g^{-1} for the symmetric configuration. The slight difference can be ascribed to resistance from current collectors, and separators in device set up. These findings suggest that the WB700 obtained via the MBCA approach, is a promising alternative electrode material for supercapacitor applications.

Further scanning of WB700 electrode at scan rates up to 200 mV/s (Fig. 4c), revealed a quasi-rectangular shape, signifying excellent rate performance and stability. Similar trend was observed in WB800 and WB900 (see supplementary materials). Thus, the reaction kinetics for WB700 was analysed using the Trasatti method (Sun et al., 2023) based on CVs that lacked redox peaks and are presented in Fig. 4d-e. Various capacitance contribution was calculated using equations (6–8), yielding $C_t = 357.14$F g^{-1}, C_{EDL}=232.46F g^{-1}, and $C_{pseudo} = 124.68$F g^{-1}. These values confirm the co-existence of surface confinement and diffusion control process in the WB700 carbon, which cannot be distinctly separated in a supercapacitor device (Chen, 2021). Furthermore, the C_{EDL} value, 1.86 times that of C_{pseudo}, confirms that the EDL charge storage mechanism is predominant, aligning with the CV (Fig. 4c). The contributions of C_{EDL}, and C_{pseudo} to the total capacitance were determined to be 65.1 % and 35.9 %, respectively. It should be noted that the C_{pseudo} contribution is attributed to a linear pseudo capacitance phenomenon,

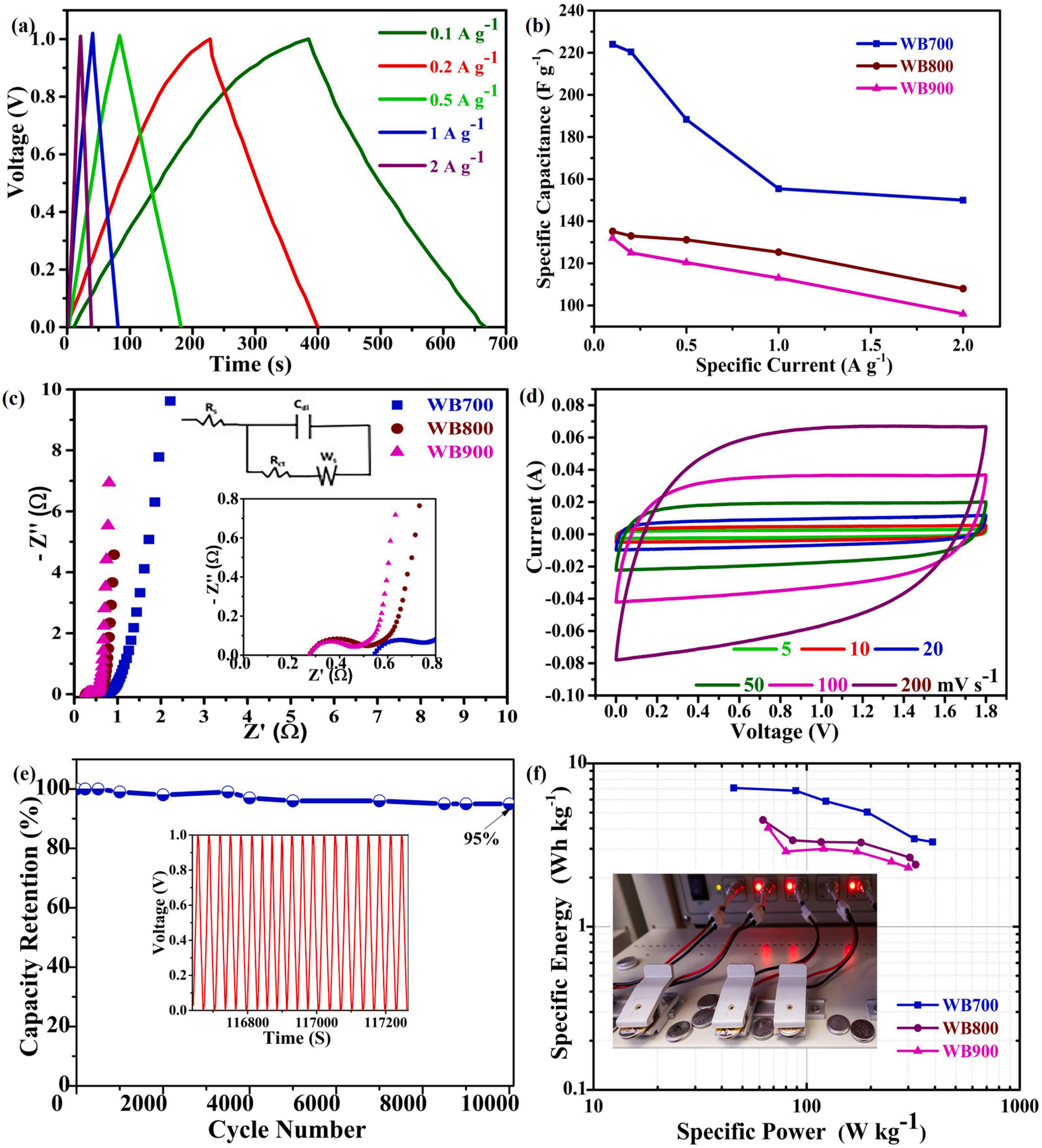

Fig. 5. (a) GCD curves at various specific currents for WB700, (b) Calculated specific capacitance from GCD for WB700, WB800, and WB900 at various specific currents in 6 M KOH, (c) Nyquist plot of WB700, WB800, and WB900 in EDL capacitors (Inset: Randle's circuit for modelling the resistance of cells, with an expanded view of the Nyquist plot), (d) CVs of WB700 at different scan rates from 5 to 200 mV/s in 1 M $TEABF_4$/AN electrolyte, (e) Cycling stability and capacitance retention of WB700 at 2 A/g (Inset: GCD curves for the cell), and (f) Ragone plot for WB700, WB800, and WB900 (Inset: photo of devices charging).

as evidenced by the rectangular CVs and linear GCDs (Fig. 4 b, and 5 a).

Furthermore, the linear decrease in specific capacitance with increasing scan rates (Fig. 4f) suggests rapid mass diffusion of ions at the electrode interface of carbon samples (Pang et al., 2021). Notably, the similar specific capacitance at 200 mV/s for WB800 and WB900 is attributed to their similar mesoporous structure (Fig. 3b), which allows for efficient ion transport within the carbon, particularly at high scan rates, despite the differences in SSA. This behaviour further proves that electrochemically active surface area of carbon affects its performance. The overall superior specific capacitance observed for WB700 is linked to its hierarchical ultra micropores, super micropore structure, and surface properties, as previously discussed.

GCD measurements at various specific currents revealed symmetrical triangular GCD curves with linear discharge (Fig. 5**a**), confirming the predominant EDL charge storage mechanism revealed by CV. Similar behaviour was observed for WB800 and WB900 (see supplementary materials). The IR drop in the GCD curves is indicative of typical EDL behaviour with low ion diffusion resistance (Sangtong et al., 2021; Zou et al., 2018). The differences in discharge time at different specific currents for WB700, WB800, and WB900 reflect the impact of their microstructures and pore connectivity (Fig. 2**d-f**), which influences ion diffusion at the electrode/electrolyte interface during charge/discharge (Choudhury et al., 2022). The calculated specific capacitance values at 2 A/g using equation (3), were 150F g^{-1}, 108F g^{-1}, and 96F g^{-1} for WB700, WB800, and WB900, respectively. The high specific capacitance of WB700 is attributed to the presence of ultra micropores (<0.7 nm) and a micropore size of 1.94 nm for accommodating electrolyte-solvated ions, thereby enhancing capacitance (Heimböckel et al., 2019; Zhong, et al., 2015). Furthermore, the linear decrease in specific capacitance with increasing specific currents (Fig. 5**b**) further supports the CV results and shows the excellent rate performance of the samples.

The specific capacitance of WB700, derived from the MBCA is comparable to that of other biomass sources subjected to multiple thermal stages with higher KOH ratios. For instance, rubber wood sawdust waste achieved 195F g^{-1} after carbonisation and activation with KOH at a KOH-to-char ratio of 4:1 (Sangtong et al., 2021). Pomelo peel derived carbon exhibited 219F g^{-1} following cryodesiccation, carbonisation, and activation with KOH at a KOH-to-biomass ratio of 4:1 ratio (Li et al., 2021). Waste tobacco straw, processed by ball milling, carbonisation, and activation with nano-ZnO at a ZnO-to-biomass ratio of 1:1, resulted in 220F g^{-1} (Jiang et al., 2022). Chili straw waste obtained 352F g^{-1} after carbonisation and microwave activation at a 4:1 mass ratio of KOH-to-biomass. Bamboo shoot shells, processed through hydrothermal treatment, H_2SO_4, carbonisation with Melamine, and activation with KOH at a 2:1 KOH-to-biomass ratio, yielded 209F g^{-1} (Huang et al., 2019).

To investigate the electrolyte ion transfer mechanism, ESI was conducted, and the results were illustrated in the Nyquist plot (Fig. 5c). The data was analysed using Randle's circuit model (Fig. 5c insert). WB700 exhibited the highest interfacial electrolyte resistance (Rs), with a value of 0.50 Ω, compared to 0.24 Ω for WB800 and 0.25 Ω for WB900. These results suggest that the increased resistance in WB700 is linked to its high content of hydroxyl (O-H), carbonyl, and carboxyl groups (O-C=O or COOH), as revealed by XPS in Fig. 4**c** and TGA (see supplementary materials). Moreover, these functional groups have shown to affect carbon behaviour towards electrolyte penetration (Ding, et al., 2019; Tekin & Topcu, 2024). The charge transfer resistance (R_{ct}), indicative of electrochemical kinetics and stability, was 0.24 Ω, 0.28 Ω, and 0.26 Ω for WB700, WB800, and WB900, respectively. Notably, the lowest R_{ct} value for WB700 suggests rapid charge and ion transport within the porous electrode. These results imply that the high nitrogen and oxygen content in WB700 was favourable for enhancing the wettability of the electrode and ion diffusion. In the high-frequency region, WB700 exhibited a higher diffusion resistance compared to WB800 and WB900, which was clear in its higher near-vertical line. This diffusion behaviour is attributed to its narrow pore size and high nitrogen and oxygen content of WB700, which contribute to obtain high capacitance. This finding aligns with the CV results and further confirms the existence of a linear pseudo-capacitance contribution.

To assess practical use of WB700, a symmetric cell was assembled using commercial organic electrolytes (1 M $TEABF_4$/AN), with CV shown in Fig. 5d. The quasi-rectangular CV devoid of redox peaks up to 200 mVs^{-1}, further confirms that EDL capacitive mechanism is predominant, showing favourable compatibility with the electrolyte. This compatibility is likely due to its stable oxygen functional groups, which enhance the carbon-electrolyte wettability (Ding et al., 2019). The calculated specific capacitance using equation (2) was 182F g^{-1} at 5 mVs^{-1}. Compared to 327F g^{-1} in 6 M KOH, the difference highlights the impact of electrolyte ion size, hydration shells, and the conductivity differences between aqueous and organic electrolytes (Heimböckel et al., 2019; Simon & Gogotsi, 2013; Yang et al., 2019a). These findings suggest WB700 could serve as an active electrode material for commercial supercapacitors.

Long cycle stability is crucial for electrode materials, and WB700 exhibited this with 10,000 cycles at 2 A/g, while retaining 95 % of its initial capacitance (Fig. 5e). The impressive cyclability is attributed to the stable nitrogen groups within the carbon structure, which enhanced the reversibility of charge-carrying ions over extended cycles (Zou et al., 2018; Sun et al., 2023). To further demonstrate the application of the derived carbon samples, the specific energy and power of the devices were calculated using equations (4–5) and depicted in the Ragone plot (Fig. 5f). At 2 A/g, WB700 exhibited the highest specific energy and power, reaching 3.45 Wh kg^{-1} and 600 W kg^{-1}, respectively. These values are impressive considering the voltage window of 1 V for the KOH electrolyte, as the specific energy and power of devices have shown to be dependent on the voltage window of electrolytes (Kondrat et al., 2012). Furthermore, these values fall within the typical range of 1 to 1000 Wh kg^{-1} and 100 to 100,000 W kg^{-1} for specific energy and power in commercial supercapacitors that utilise organic electrolytes (Raut et al., 2010). However, further research should focus on improving the specific energy while maximising its capacitive performance.

4. Conclusion

This study introduces a straightforward MBCA process to produce electrode carbon from biomass through single-stage heating with low amount of reagent. It uses KOH and biomass inherent moisture to alter the components' structure via dehydration and nucleophilic reactions to produce organic salts before drying. These salts promote in-situ activation to yield a carbon with 327F $g^{-}1$ capacitance and 95 % cycling stability over 10,000 cycles at 2 A/g, due to its suitable SSA, ultra micropores, and surface properties. The MBCA approach merits extension to other high-moisture biomass sources for energy storage applications, highlighting its innovative capacity.

CRediT authorship contribution statement

Ishioma Laurene Egun: Writing – original draft, Methodology, Investigation, Conceptualization. **Bamidele Akinwolemiwa:** Formal analysis. **Bo Yin:** Formal analysis. **Hai Tian:** Formal analysis. **Haiyong He:** Supervision, Resources. **Kam Loon Fow:** Writing – review & editing. **Honglei Zhang:** Writing – review & editing. **George Z. Chen:** Supervision. **Di Hu:** Writing – review & editing, Supervision, Resources.

Declaration of competing interest

The authors declare that they have no known competing financial interests or personal relationships that could have appeared to influence the work reported in this paper.

Data availability

Data will be made available on request.

Acknowledgements

This work was supported by the Doctoral Training Programme of the University of Nottingham Ningbo China and the Ningbo Institute of Materials Technology & Engineering, CAS, China.

Appendix A. Supplementary data

Supplementary data to this article can be found online at https://doi.org/10.1016/j.biortech.2024.131251.

References

Ahn, K., Zaccaron, S., Zwirchmayr, N.S., Hettegger, H., Hofinger, A., Bacher, M., Henniges, U., Hosoya, T., Potthast, A., Rosenau, T., 2019. Yellowing and brightness reversion of celluloses: CO or COOH, who is the culprit? Cellulose 26 (1), 429–444.

Bhaumik, A., Haque, A., Taufique, M., Karnati, P., Patel, P., Nath, N., Ghosh, K., 2017. Reduced graphene oxide thin films with very large charge carrier mobility using pulsed laser deposition. J. Mater. Sci. Eng. 6, 364.

Cao, J., Luo, J., Wang, P., Wang, X., Weng, W., 2019. Biomass-based porous carbon beehive prepared in molten KOH for capacitors. Mater. Technol. 35 (9–10), 522–528.

Celiktas, M.S., Alptekin, F.M., 2019. Conversion of model biomass to carbon-based material with high conductivity by using carbonization. Energy. 188, 116089.

Chen, G.Z., 2021. Linear and non-linear pseudocapacitances with or without diffusion control. Prog. Nat. Sci.: Mater. Int. 31 (6), 792–800.

Chen, C., Cheng, G., Liu, Y., Yi, Y., Chen, D., Zhang, L., Wang, X., Cao, J., 2022. Correlation between microorganisms and flavor of Chinese fermented sour bamboo shoot: roles of Lactococcus and Lactobacillus in flavor formation. Food Biosci. 50, 101994.

Chen, W., Gong, M., Li, K., Xia, M., Chen, Z., Xiao, H., Fang, Y., Chen, Y., Yang, H., Chen, H., 2020. Insight into KOH activation mechanism during biomass pyrolysis: chemical reactions between O-containing groups and KOH. Appl. Energy. 278, 115730.

Choudhury, B.J., Muigai, H.H., Kalita, P., Moholkar, V.S., 2022. Biomass blend derived porous carbon for aqueous supercapacitors with commercial-level mass loadings and enhanced energy density in redox-active electrolyte. Appl. Surf. Sci. 601, 154202.

Chung, H.Y., Pan, G.T., Hong, Z.Y., Hsu, C.T., Chong, S., Yang, T.C., Huang, C.M., 2020. Biomass-derived porous carbons derived from soybean residues for high performance solid state supercapacitors. Molecules. 25 (18).

Ding, Z., Trouillet, V., Dsoke, S., 2019. Are functional groups beneficial or harmful on the electrochemical performance of activated carbon electrodes? J. Electrochem. Soc. 166 (6), 1004–1014.

Egun, I.L., He, H., Hu, D., Chen, G.Z., 2022. Molten salt carbonization and activation of biomass to functional biocarbon. Adv. Sustain. Syst. 6, 2200294.

Ghazanfar, M., Irfan, M., Nadeem, M., Shakir, H.A., Khan, M., Ahmad, I., Saeed, S., Chen, Y., Chen, L. 2022. Bioethanol Production Optimization from KOH-Pretreated Bombax ceiba Using Saccharomyces cerevisiae through Response Surface Methodology. in: Fermentation. Vol. 8.

Gu, L., Zhou, Y., Mei, T., Zhou, G., Xu, L., 2019. Carbon footprint analysis of bamboo scrimber flooring—implications for carbon sequestration of bamboo forests and its products. Forests. 10 (1), 51.

Heimböckel, R., Hoffmann, F., Fröba, M., 2019. Insights into the influence of the pore size and surface area of activated carbons on the energy storage of electric double layer capacitors with a new potentially universally applicable capacitor model. Phys. Chem. Chem. Phys. 21 (6), 3122–3133.

Hu, M., Ye, Z., Zhang, Q., Xue, Q., Li, Z., Wang, J., Pan, Z., 2022. Towards understanding the chemical reactions between KOH and oxygen-containing groups during KOH-catalyzed pyrolysis of biomass. Energy. 245, 123286.

Huang, G., Wang, Y., Zhang, T., Wu, X., Cai, J., 2019. High-performance hierarchical N-doped porous carbons from hydrothermally carbonized bamboo shoot shells for symmetric supercapacitors. J. Taiwan Inst. Chem. Eng. 96, 672–680.

Ilnicka, A., Skorupska, M., Szkoda, M., Zarach, Z., Kamedulski, P., Zielinski, W., Lukaszewicz, J.P., 2021. Combined effect of nitrogen-doped functional groups and porosity of porous carbons on electrochemical performance of supercapacitors. Sci. Rep. 11 (1), 18387.

Jiang, B., Cao, L., Yuan, Q., Ma, Z., Huang, Z., Lin, Z., Zhang, P., 2022. Biomass straw-derived porous carbon synthesized for supercapacitor by ball milling. Materials 15 (3).

Kondrat, S., Presser, V., Gogotsi, Y., Kornyshev, A.A., 2012. Effect of pore size and its dispersity on the energy storage in nanoporous supercapacitors. Energy Environ. Sci. 5, 6474–6479.

Krylova, A.Y., Zaitchenko, V.M., 2018. Hydrothermal carbonization of biomass: a review. Solid Fuel Chem. 52 (2), 91–103.

Li, M., Li, Y.-W., Cai, Q.-Y., Zhou, S.-Q., Mo, C.-H., 2020. Spraying carbon powder derived from mango wood biomass as high-performance anode in bio-electrochemical system. Bioresour. Technol. 300, 122623.

Li, J., O'Shea, J., Hou, X., Chen, G.Z., 2017. Faradaic processes beyond Nernst's law: density functional theory assisted modelling of partial electron delocalisation and pseudo capacitance in graphene oxides. Chem. Comm. 53 (75), 10414–10417.

Li, Y., Sun, Z., Zhang, L., Zou, Y., Yao, N., Lei, W., Jiang, T., Chen, Y., Chen, G.Z., 2021. High yield and packing density activated carbon by one-step molecular level activation of hydrophilic pomelo peel for supercapacitors. J. Electrochem. Soc. 168 (6), 060521.

Liu, J., Wu, L., Wang, R., Xue, X., Wang, D., Liang, J., 2024. Evaluation of biomass sources on the production of biofuels from lignocellulosic waste over zeolite catalysts. Bioresour. Technol. 398, 130510.

Luo, H., Yang, Y., Zhao, X., Zhang, J., Chen, Y., 2015. 3D sponge-like nanoporous carbons via a facile synthesis for high-performance supercapacitors: direct carbonization of tartrate salt. Electrochim. Acta. 169, 13–21.

Lyu, L., Seong, K.D., Ko, D., Choi, J., Lee, C., Hwang, T., Cho, Y., Jin, X., Zhang, W., Pang, H., 2019. Recent development of biomass-derived carbons and composites as electrode materials for supercapacitors. Mater. Chem. Front. 3 (12), 2543–2570.

Pang, Z., Li, G., Xiong, X., Ji, L., Xu, Q., Zou, X., Lu, X., 2021. Molten salt synthesis of porous carbon and its application in supercapacitors: a review. J. Energy Chem. 61, 622–640.

Poonam, S., Shalini, G.R., Ranjay, K.S., Santosh, S., Naik, S.N., 2018. Impact of drying techniques on physical quality of bamboo shoots: Implications on tribal's livelihoods. Indian J. Tradit. Knowl. 17 (2), 353–359.

Raut, A.S., Parker, C.B., Glass, J.T., 2010. A method to obtain a Ragone plot for evaluation of carbon nanotube supercapacitor electrodes. J. Mater. Res. 25 (8), 1500–1506.

Sangtong, N., Chaisuwan, T., Wongkasemjit, S., Ishida, H., Redpradit, W., Seneesrisakul, K., Thubsuang, U., 2021. Ultrahigh-surface-area activated biocarbon based on biomass residue as a supercapacitor electrode material: Tuning pore structure using alkalis with different atom sizes. Micropor. Mesopor. Mater. 326, 111383.

Senthil, C., Park, J.W., Shaji, N., Sim, G.S., Lee, C.W., 2022. Biomass seaweed-derived nitrogen self-doped porous carbon anodes for sodium-ion batteries: insights into the structure and electrochemical activity. J. Energy Chem. 64, 286–295.

Shen, Y., 2018. K-looping catalytic pyrolysis of unaltered and pelletized biomass for in situ tar reduction and porous carbon production. Sustain. Energy Fuels. 2 (12), 2770–2777.

Simon, P., Gogotsi, Y., 2013. Capacitive energy storage in nanostructured carbon electrolyte systems. Acc. Chem. Res. 46, 1094–1103.

Sun, Z., Zhang, M., Yin, H., Hu, Q., Krishnan, S., Huang, Z., Qi, H., Wang, X., 2023. Tailoring hierarchically porous structure of biomass-derived carbon for high-performance supercapacitors. Renew. Energy. 219, 119375.

Tekin, B., Topcu, Y., 2024. Novel hemp biomass-derived activated carbon as cathode material for aqueous zinc-ion hybrid supercapacitors: synthesis, characterization, and electrochemical performance. J. Energy Storage. 77, 109879.

Wan, C., Lu, Y., Jiao, Y., Cao, J., Sun, Q., Jian, L., 2015. Preparation of mechanically strong and lightweight cellulose aerogels from cellulose-NaOH/PEG solution. J. Sol-Gel Sci Technol. 74, 256–259.

Wang, G., Lai, D., Xu, X., Wang, Y., 2022. Lightweight, stiff and heat-resistant bamboo-derived carbon scaffolds with gradient aligned microchannels for highly efficient EMI shielding. J. Chem. Eng. 446, 136911.

Wei, Y., Jia, C.Q., 2015. Intrinsic wettability of graphitic carbon. Carbon 87, 10–17.

Yang, H., Ye, S., Zhou, J., Liang, T. 2019. Biomass-derived porous carbon materials for supercapacitor. Front. Chem. 7.

Yang, J., He, Q., Yang, L., 2019b. A review on hydrothermal co-liquefaction of biomass. Appl. Energy. 250, 926–945.

You, X., Misra, M., Gregori, S., Mohanty, A., 2018. Preparation of an electric double layer capacitor (EDLC) using miscanthus-derived biocarbon. ACS Sust. Chem. Eng. 6, 318–324.

Zdravkov, B., Čermák, J., Šefara, M., Janků, J., 2007. Pore classification in the characterization of porous materials: a perspective. Cent. Eur. J. Chem. 5 (2), 385–395.

Zhong, C., Deng, Y., Hu, W., Qiao, J., Zhang, L., Zhang, J., 2015. A review of electrolyte materials and compositions for electrochemical supercapacitors. Chem. Soc. Rev. 44, 7484–7539.

Zhu, X., Gao, Y., Yue, Q., Song, Y., Gao, B., Xu, X., 2018. Facile synthesis of hierarchical porous carbon material by potassium tartrate activation for chloramphenicol removal. J. Taiwan Inst. Chem. Eng. 85, 141–148.

Zhu, X., Sun, M., Zhu, X., Guo, W., Luo, Z., Cai, W., Zhu, X., 2023. Molten salt shielded pyrolysis of biomass waste: Development of hierarchical biochar, salt recovery, CO_2 adsorption. Fuel. 334, 126565.

Zou, K., Deng, Y., Chen, J., Qian, Y., Yang, Y., Li, Y., Chen, G., 2018. Hierarchically porous nitrogen-doped carbon derived from the activation of agriculture waste by potassium hydroxide and urea for high-performance supercapacitors. J. Power Sources. 378, 579–588.

Zou, Z., Liu, T., Jiang, C., 2019. Highly mesoporous carbon flakes derived from a tubular biomass for high power electrochemical energy storage in organic electrolyte. Mater. Chem. Phys. 223, 16–23.

Further reading

Rouquerol, J., Avnir, D., Fairbridge, C.W., Everett, D.H., Haynes, J.M., Pernicone, N., Ramsay, J.D.F., Sing, K.S.W., Unger, K.K. 1994. Recommendations for the characterization of porous solids (Technical Report). 66(8), 1739-1758.